Fe-doped LiMnPO₄@C nanofibers with high Li-ion diffusion coefficient

Hao Yang, Cuimei Fu, Yijian Sun, Lina Wang[*], Tianxi Liu[**]

State Key Laboratory for Modification of Chemical Fibers and Polymer Materials, College of Materials Science and Engineering, Innovation Center for Textile Science and Technology, Donghua University, Shanghai, 201620, China

ARTICLE INFO

ABSTRACT

Olivine-type LiMnPO₄ (LMP) cathodes have gained enormous attraction for Li-ion batteries (LIBs) due to high discharge platform, theoretical capacity and thermal stability. However, it is still challenging to achieve encouraging Li-storage behavior owing to the low electronic conductivity and slow Li-ion diffusion rate of LMP. Here, the electrochemical behavior of fibrous LiFe$_x$Mn$_{1-x}$PO₄@carbon (LF$_x$M$_{1-x}$P@C, x = 0, 0.25, 0.5, 0.75, 1) composites with different Fe doping amounts is investigated. Among the composites, LF$_{0.5}$M$_{0.5}$P@C demonstrates a superior cell performance due to a higher Li-ion diffusion coefficient (D_{Li}), resulting from a proper Fe doping ratio and a more uniform morphology. At a current rate of 0.2 C (1 C = 170 mA g^{-1}), the LF$_{0.5}$M$_{0.5}$P@C cathode delivers a specific capacity of 150 mAh g^{-1} up to 500 cycles with a capacity retention of 119%. A longer-term cycling at 5 C for 2000 cycles can be maintained with a reversible capacity exceeding 102 mAh g^{-1}. The fundamental study provides an insightful guidance for future design of cathode materials with high performance.

© 2019 Elsevier Ltd. All rights reserved.

1. Introduction

The application of Li-ion batteries (LIBs) in hybrid and electric vehicles has attracted considerable academic and industrial research interest [1–3]. Since the pioneering work by Goodenough group in 1997 [4–7], the cathode materials of olivine-structured lithium transition-metal phosphates (LiMPO₄, M = Fe, Mn, Co and Ni) have been extensively studied due to high theoretical capacity, thermal stability and environmental friendliness. The strong covalent P—O bonds in the poly-anion units can effectively inhibit oxygen loss and provide high structural stabilization, which is helpful to increase cycle life and weaken the polarization phenomenon [8,9]. In particular, on the basis of safety requirement, LiFePO₄ (LFP) has been successfully used in LIBs. As an alternative, LiMnPO₄ (LMP) provides the same theoretical specific capacity (170 mAh g^{-1}) but a higher redox potential of Mn^{2+}/Mn^{3+} (4.1 V vs. Li/Li$^+$) in comparison to Fe^{2+}/Fe^{3+} (3.4 V vs. Li/Li$^+$), thus leading to a ~20% higher theoretical energy density of LMP (701 Wh kg^{-1}) than that of LFP (586 Wh kg^{-1}) [10,11]. Despite these merits, LMP with dramatically enhanced power density combined with high specific capacity and long-term cyclic stability is still hardly acquired. The

very low levels of ionic diffusivity (10^{-16}–10^{-14} cm^2 s^{-1}) and electrical conductivity (<10^{-9} S cm^{-1}) slow down its electrochemical activities [12]. In addition, the phase boundary mobility affected by the anisotropically large lattice mismatch between the lithiation and delithiation phases, the small polaronic conductivity of Jahn-Teller active Mn^{3+}, etc., are known as the possible origins of the sluggish kinetics [13,14].

The electrochemical redox reaction of the electrode depends on the kinetics of de-intercalation/intercalation of Li$^+$ and the loss/gain of electrons at the interface between electrode and electrolyte. As a result, the transport of electrons and Li$^+$ to or from the active particles and the rate of Li$^+$ insertion within the bulk material are key factors influencing the rate capability. Carbon-coating as a commonly used and highly effective practice has successfully improved the transport of electrons to the active particles [4,6,8,11,15,16]. In a micron-sized battery material, the kinetics of charge storage is generally controlled by the diffusion of Li$^+$ within the bulk particles. Therefore, the reaction kinetics can be improved through nanostructuring of a battery material [15,17]. The substitution of the Mn-site with a suitable amount of Fe is another approach to activate LMP. Fe doping was thought can alleviate Jahn-Teller distortion of Mn^{3+} due to the super exchange interaction between Fe^{3+}—O—Mn^{2+}, leading to the stabilized crystal structure and enhanced charge transfer [18,19]. The work by Zhao et al. showed a plate-like LiFe$_{0.5}$Mn$_{0.5}$PO₄/C with a Li-ion diffusion coefficient (D_{Li}) of 8.46×10^{-15} cm^{-2} s^{-1} delivering a discharge capacity of 78 mAh g^{-1}

at 5 C (1 C = 170 mA g^{-1}) [20]. Liu et al. reported LiMn$_{0.8}$Fe$_{0.2}$PO$_4$/Fe/C nanorods with a D$_{Li}$ of 2.15 × 10^{-14} cm^{-2} s^{-1} delivering a specific discharge capacity of 76 mAh g^{-1} at 10 C [21]. Saravanan et al. prepared LiMn$_{0.7}$Fe$_{0.3}$PO$_4$/C nanorods with a D$_{Li}$ ~10^{-13} cm^{-2} s^{-1}, achieving a discharge capacity of 119 mAh g^{-1} at 5 C [22]. Although the significant progress on the Fe doped LMP materials, the effect of Fe doping amounts and the related mechanism need further exploration. A simpler and more effective synthesis is also in urgent need.

Here, we report a rational design and fabrication of a series of fibrous LiFe$_x$Mn$_{1-x}$PO$_4$@carbon (LF$_x$M$_{1-x}$P@C, x = 0, 0.25, 0.5, 0.75, 1) composites via a facile and versatile electrospinning strategy. We further demonstrate the relationship between D$_{Li}$ and Fe doping amount. A high D$_{Li}$ of 3.31 × 10^{-12} cm^{-2} s^{-1} is achieved when x = 0.5, leading to a high reversible capacity and rate capability upon long-term cycling. A discharge capacity of 150 mAh g^{-1} is reached after 500 cycles at 0.2 C with a capacity retention of 119%. At a high rate of 5 C, a specific capacity of 102 mAh g^{-1} can still be afforded even over 2000 cycles with a CE ≥ 99%, making it a promising cathode material for LIBs.

2. Experimental

2.1. Synthesis of LF$_x$M$_{1-x}$P@C nanofibers

LiH$_2$PO$_4$ (99%, Aladdin), FeSO$_4$·7H$_2$O (99%, Sinopharm), MnSO$_4$·H$_2$O (99%, Sinopharm), citric acid (99.5%, Aladdin), CH$_3$CH$_2$OH (99.8%, Sinopharm) and polyvinylpyrrolidone (PVP, M$_w$ = 1300000, Sigma-Aldrich) were used as received. LF$_x$M$_{1-x}$P@C nanofibers were synthesized by one-step electrospinning technique followed by a heat-treatment. Typically, 6 mmol LiH$_2$PO$_4$, FeSO$_4$·7H$_2$O, MnSO$_4$·H$_2$O was dispersed in 8 mL of deionized water under vigorous stirring at 30 °C for 2 h. Afterward, 240 mg citric acid and 1 g PVP was added under vigorous stirring at 30 °C for 1 h. Finally, 2 mL of ethanol was added and stirred overnight at 30 °C. The ratios of Fe/Mn was adjusted by stoichiometric mixing of FeSO$_4$·7H$_2$O and MnSO$_4$·H$_2$O. The precursor solution was transferred into a syringe with a 10-gauge blunt-tip needle for electrospinning. The flow rate of solution controlled by a syringe pump was approximately 0.8 μL min^{-1}, and a grounded aluminum foil was horizontally placed 20 cm from the needle to collect the nanowires. A voltage of 15 kV was applied by a high-voltage power supply. The dried precursor fibers were calcined at 750 °C for 6 h in an argon (Ar) atmosphere at a rate of 5 °C min^{-1}.

2.2. Material characterizations

The morphology of LF$_x$M$_{1-x}$P@C was observed by field-emission scanning electron microscopy (FE-SEM, S-4800, HITACHI). High-resolution transmission electron microscopy (HR-TEM) and selected-area electron diffraction (SAED) measurements were also carried out on a transmission electron microscope (JEOL JEM-2100F). The crystalline structure of the samples was characterized by an X-ray diffractometer (XRD, D/max-2500VB+/PC, Rigalcu) equipped with a Cu-Kα radiation at a scan rate of 4° min^{-1}. Raman spectra were detected by a Raman Spectrometer (inVia-Reflex, Renishaw). X-ray photoelectron spectroscopy (XPS) analyses were performed on a spectrometer (Escalab 250Xi) with Al Kα X-ray radiation. Thermogravimetry (TG) was conducted on a TG-DSC analyzer (NETZSCH TG 209 F1 Libra).

2.3. Electrochemical measurements

In preparing the electrodes, black viscous slurry made from 80 wt% LF$_x$M$_{1-x}$P@C, 10 wt% Ketjenblack carbon (KB carbon, ECP-600JD) and 10 wt% poly (vinylidene fluoride) (PVdF) in *N*-methyl-2-pyrrolidone (NMP) was cast onto an aluminum foil. The electrodes were then dried under vacuum at 120 °C overnight to remove NMP before punched into disks with a diameter (d) of 12.0 mm. The cells were assembled in an Ar-filled glove box (Mikrouna Universal) using CR2025-type coin cells. High-purity metallic lithium anode (d = 14 mm, 0.3 mm thick) was separated from the cathode using a Celgard separator (d = 18 mm, 25 μm thick). The electrolyte is 1.0 M LiPF$_6$ dissolved in ethylene/dimethyl carbonate/diethyl carbonate (EC/DMC/DEC, 1:1:1, v/v). The assembled cells were galvanostatically charged–discharged in voltage range of 2.0–4.5 V (vs. Li/Li$^+$) on a LAND battery testing system (CT2001A) under room temperature. The applied current densities and specific capacity were calculated based on the mass of LF$_x$M$_{1-x}$P. The average loading of LF$_x$M$_{1-x}$P is approximately 3 mg cm^{-2}. Cyclic voltammetry (CV) tests were measured by electrochemical workstation (Arbin Instruments, USA). Electrochemical impedance spectra (EIS) with an AC perturbation signal of 5.0 mV in the frequency range of 100 kHz–100 mHz were recorded on a CHI660C electrochemical workstation (Shanghai Chenhua, China).

3. Results and discussion

3.1. Synthesis and characterizations of LF$_x$M$_{1-x}$P@C nanofibers

The as-spun fibers were obtained by electrospinning a solution of PVP containing LiH$_2$PO$_4$, FeSO$_4$·7H$_2$O, MnSO$_4$·H$_2$O, citric acid and CH$_3$CH$_2$OH. Whereby, PVP provides the desirable rheological properties as well as serving as a carbon source. Citric acid acting as a chelating agent to promote dissolution of the metal salts. CH$_3$CH$_2$OH with a low surface tension (21.97 mN m^{-1} at 25 °C) increases the spinnability of precursor. The as-spun fibers were thermally treated in an Ar atmosphere at 750 °C for 6 h to obtain LF$_x$M$_{1-x}$P@C composites. The crystalline structure of the LF$_x$M$_{1-x}$P@C was examined by XRD (Fig. 1a). All of the diffraction peaks are indexed to the olivine structure of the standard LMP (JCPDS#74–0375) or LFP (JCPDS#83–2029) with a space group of Pnmb with no evidence of impurities. All of the peaks right shift as the doping amount of Fe increasing, resulting from a larger ionic radius of Mn^{2+} (0.66 Å) than that of Fe^{2+} (0.63 Å) (Fig. 1b) [17]. The lattice parameters estimated from the reflection positions using a refinement process are indicated in Fig. 1c. The lattice parameters (a, b and c) and lattice volume (V) decrease with increasing doping amount, which is also related to the increase of Fe^{2+} with a smaller ionic radius. The calculated grain size summarized in Table S1 suggests the grain size of LF$_{0.5}$M$_{0.5}$P@C is the smallest, i.e., 282 Å. It was found the spinnability of precursor solution is related to the ratio of Fe/Mn. A homogeneous solution was more readily obtained when the mole ratio of Fe/Mn is 1:1. The suitable proportion of precursor salts likely leads to a smaller grain size of LF$_{0.5}$M$_{0.5}$P@C product. A grain change model is illustrated in Fig. 1d, in which the outer gray part is a carbon layer and the inner layer is LF$_x$M$_{1-x}$P. Fig. 1e shows the crystal structural model, which consists of a polyoxyanionic framework containing LiO$_6$ octahedra, MO$_6$ octahedra and PO$_4$ tetrahedra. The unit cell volume decreases with increasing doping amount, which is in accordance with the XRD.

SEM images reveal that all of the LF$_x$M$_{1-x}$P@C composites possess a 3D network constructed from interconnected nanofibers (Fig. 2a–e). However, the morphology of the nanofibers is greatly dependent on the ratio of Fe/Mn. Uniformly interconnected smooth and long nanofibers with a mean diameter ca. 200 nm can be observed from the LMP@C, LF$_{0.5}$M$_{0.5}$P@C and LFP@C composites (Fig. 2a, c and e). Whereas, the LF$_{0.25}$M$_{0.75}$P@C and LF$_{0.75}$M$_{0.25}$P@C composites exhibit irregular nanofibers with a roughen surface (Fig. 2b and d). When x = 0.25 and 0.75, the spinnability of the
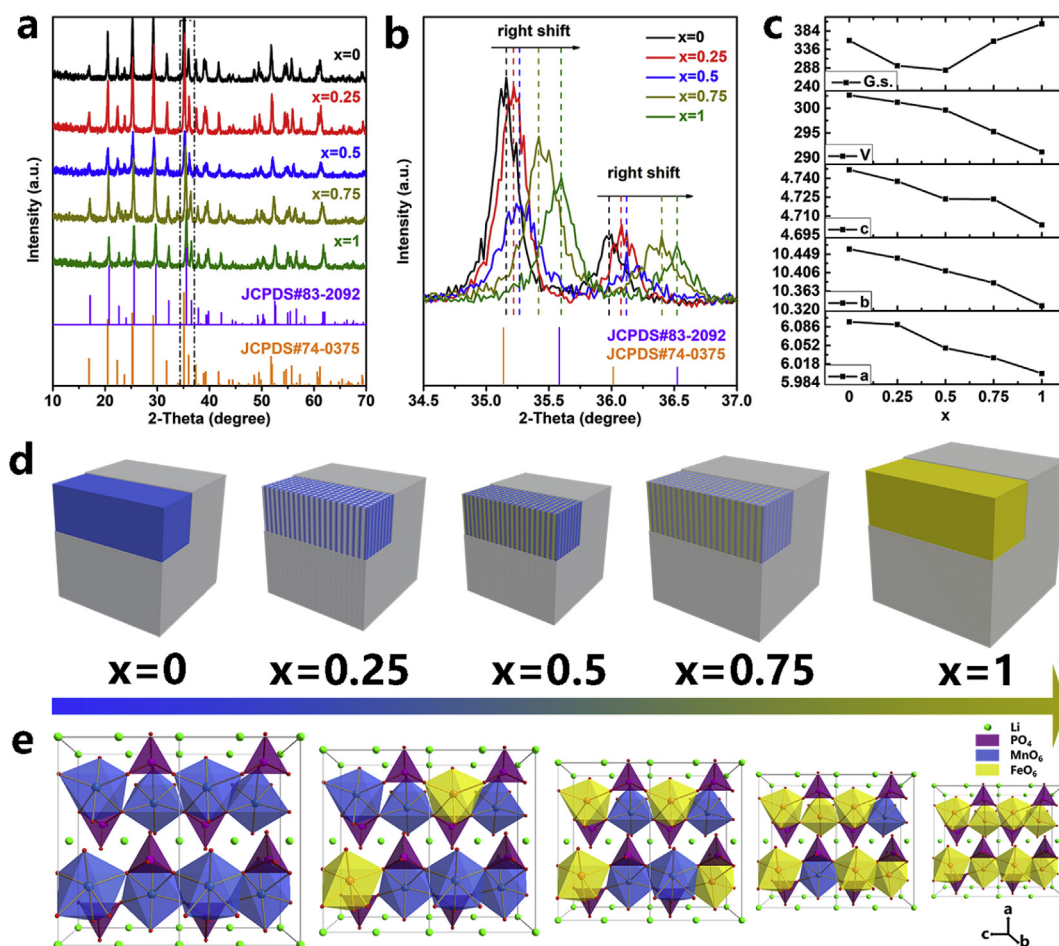
Fig. 1. (a, b) XRD pattern and magnification pattern of $LF_xM_{1-x}P@C$ composites. (c) Changes in the lattice parameters of $LF_xM_{1-x}P@C$ with increasing Fe (x) in $LF_xM_{1-x}P@C$. (d) Grain change model of $LF_xM_{1-x}P@C$. The outer gray part is a carbon layer and the inner layer is $LF_xM_{1-x}P$. (e) Crystal structure of $LF_xM_{1-x}P$. (A colour version of this figure can be viewed online.)

precursor solution was decreased somewhat, indicating the added salts were not mixed very uniformly in the solvent. The smooth surface of $LF_{0.5}M_{0.5}P@C$ can be more clearly observed on the high-resolution transmission electron microscopy (TEM) image (Fig. 2f). The clear lattice fringes with an interplanar spacings of 0.35 nm correspond to the respective (201) planes of crystalline $LF_{0.5}M_{0.5}P$ [23], which are embedded in an ultrathin carbon layer ca. 2.5 nm (Fig. 2g). The carbon is expect to enhance the electronic conductivity of the composites. TGA analysis suggests that the carbon contents in LMP@C, $LF_{0.25}M_{0.75}P@C$, $LF_{0.5}M_{0.5}P@C$, $LF_{0.75}M_{0.25}P@C$ and LFP@C are approximately 15, 19, 18, 18 and 14 wt%, respectively (Fig. S1). The uniform distribution of the Fe, Mn, P, O and C elements in the $LF_{0.5}M_{0.5}P@C$ nanofibers was identified by EDS element mapping images (Fig. 2h).

The Raman spectra of $LF_xM_{1-x}P@C$ display two peaks centered at 1353 and 1567 cm^{-1}, corresponding to the disorder induced D-band (sp^3 hybridization) and in-plane vibrational G-band (sp^2 hybridization), respectively (Fig. 3a). The disorder of carbon identified by the intensity ratio of disorder induced D-band to in-plane vibrational G-band (I_D/I_G) value in Raman spectra is in the range of 0.964–0.987, reflecting the relative high degree of ordering in the carbon material. It indicates the carbon in the composite predominately contains sp^2 type carbon, thereby enabling a good electronic conductivity [24]. XPS spectra do not show dateable difference on the elemental chemical states of these $LF_xM_{1-x}P@C$ samples. Take the $LF_{0.5}M_{0.5}P@C$ for example, the survey XPS

spectrum shows that the binding energies of Li 1s, Fe 2p, Mn 2p, P 2p, O 1s and C 1s are 50.31, 718.92, 650.15, 134.51, 531.40 and, 283.38 eV, respectively (Fig. S2). The C 1s peak is deconvoluted into C–C (284.70 eV), C–O (286.04 eV) and C=O (287.94 eV), respectively (Fig. 3b) [25,26]. In the Fe 2p spectrum, the peak at 725.00 eV corresponds to the Fe $2p_{1/2}$ of Fe^{2+}. And that at 711.10 and 714.40 eV correspond to Fe^{2+} and Fe^{3+} oxidation state, respectively, reflecting the existence of a higher oxidation state of Fe^{3+} on the surface. The energy separation between the Fe $2p_{3/2}$ (711.10 eV) and Fe $2p_{1/2}$ (725.00 eV) peaks is 13.9 eV, confirming the presence of Fe^{2+} oxidation state in the olivine type LFP [27]. The Mn 2p spectrum splits into two peaks due to spin-orbit coupling (Mn $2p_{3/2}$ and Mn $2p_{1/2}$) with a "shake-up" satellite (Fig. 3d) [28]. The peak at 653.98 eV corresponds to the Mn $2p_{1/2}$ of Mn^{2+}, while the Mn $2p_{3/2}$ spectra center at 641.52 and 642.72 eV correspond to Mn^{2+} and Mn^{3+} oxidation state, respectively, reflecting the existence of a higher oxidation state of Mn^{3+} on the surface. However, obvious Fe^{3+}/Mn^{3+} impurities are not detected from the XRD results in Fig. 1a, indicating the extremely trace amount of Fe^{3+}/Mn^{3+}. The coexistence of Fe^{3+}/Mn^{3+} should be due to the instability of Fe^{2+}/Mn^{2+} during synthesis at high temperature or when the $LF_xM_{1-x}P@C$ exposed in an ambient atmosphere [29–31]. The satellite peak at 647 eV is the characteristic peak of bivalent Mn [28,32]. The P 2p peak at 133.72 eV is attributed to the PO_4^{3-} moiety (Fig. 3e) [33]. In Fig. 3f, the fitted O 1s peaks at 533.40 and 532.47 eV are attributed to the C–O and C=O bands, respectively [34]. The peak
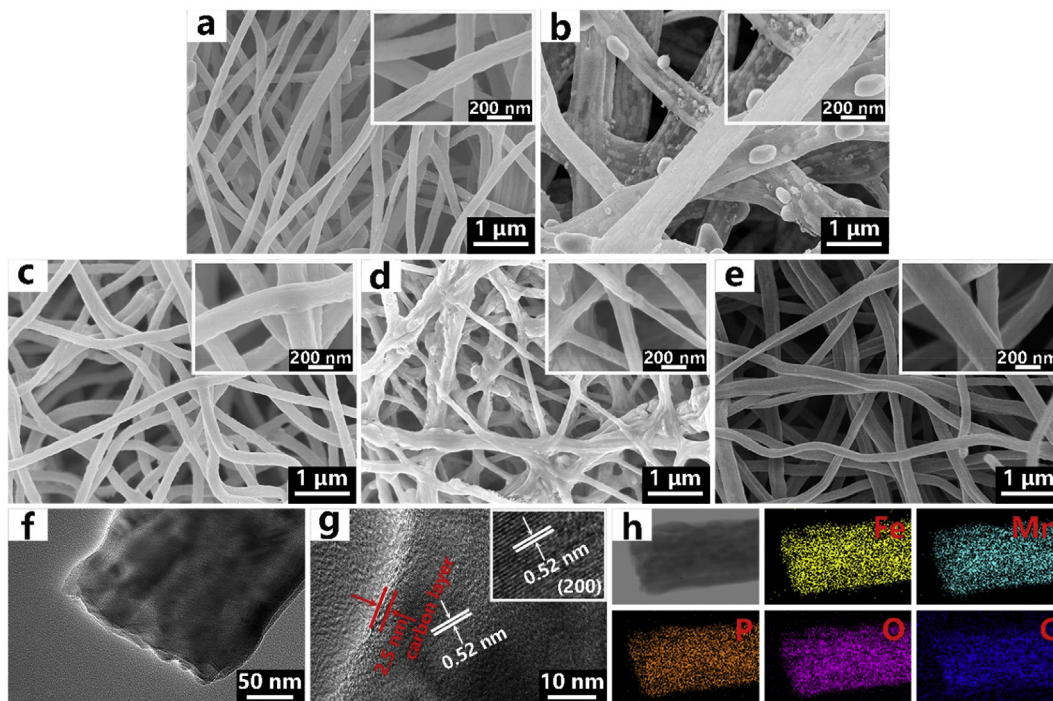
Fig. 2. Micrographs of $LF_xM_{1-x}P@C$ composites after heat-treatment at 750 °C. (a—e) SEM images of $LF_xM_{1-x}P@C$ with insets of the corresponding high-magnification images. (a) x = 0; (b) x = 0.25; (c) x = 0.5; (d) x = 0.75; (e) x = 1. (f, g) HR-TEM images of $LF_{0.5}M_{0.5}P@C$ nanofibers. The inset of (g) shows lattice fringes. (h) TEM-EDS mapping. (A colour version of this figure can be viewed online.)
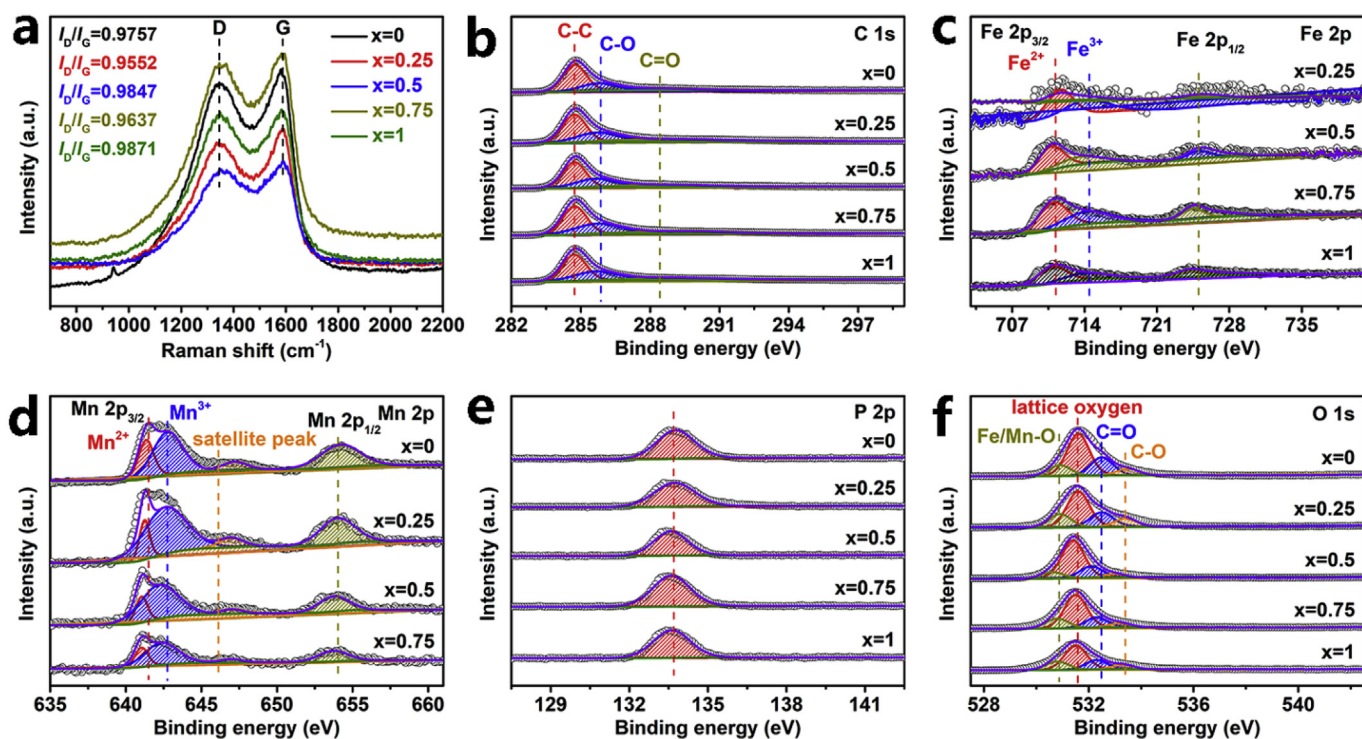

Fig. 3. (a) Raman spectra and (b—f) XPS spectra of $LF_xM_{1-x}P@C$ composites. (b) C 1s, (c) Fe 2p, (d) Mn 2p, (e) P 2p and (f) O 1s spectra. (A colour version of this figure can be viewed online.)
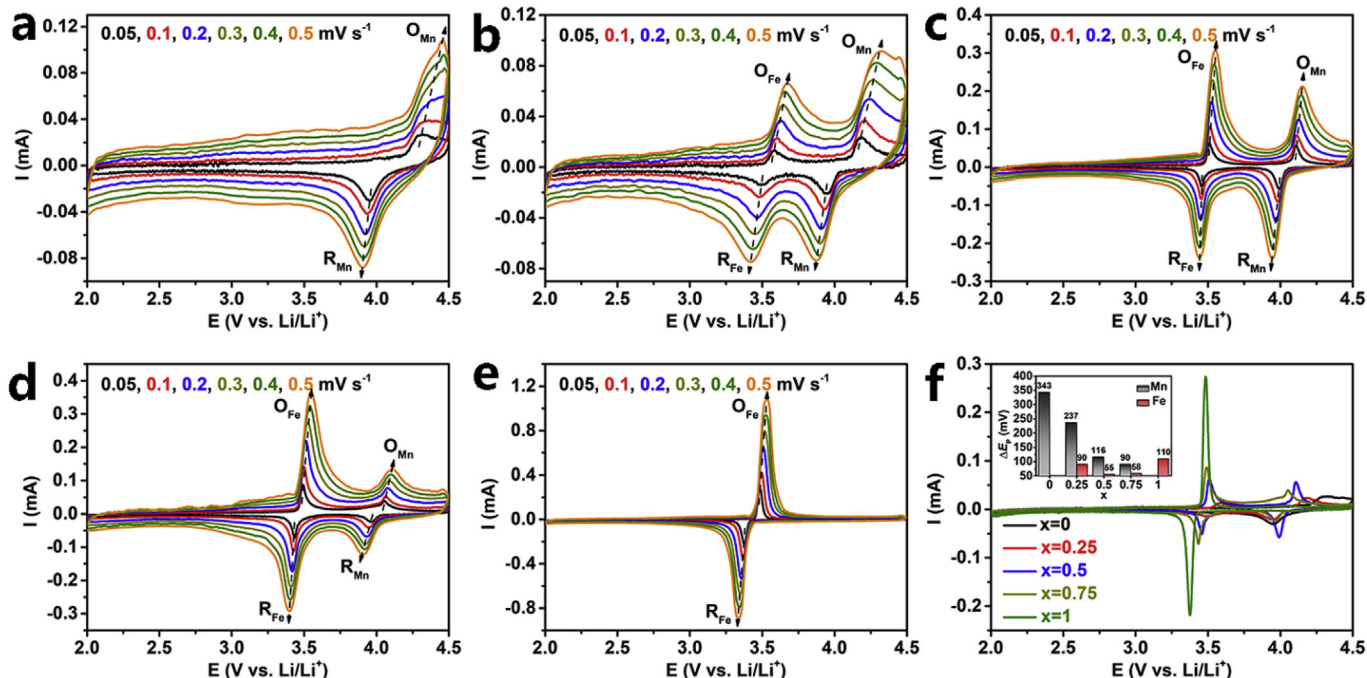
Fig. 4. (a–e) CV curves of LF$_x$M$_{1-x}$P@C electrodes at various sweep rates of 0.05, 0.1, 0.2, 0.3, 0.4 and 0.5 mV s^{-1}. (a) x = 0; (b) x = 0.25; (c) x = 0.5; (d) x = 0.75; (e) x = 1. (f) CV curves at a sweep rate of 0.05 mV s^{-1} with the inset showing the ΔE_P of LF$_x$M$_{1-x}$P@C. (A colour version of this figure can be viewed online.)

at 531.59 eV corresponds to oxygen atoms of the PO_4^{3-}. The peak near 530.86 eV is related to the Fe/Mn−O band [35].

3.2. Li$^+$ storage performance and reaction kinetics of LF$_x$M$_{1-x}$P@C nanofibers

To understand the effect of doping amount on Li$^+$ diffusion, CV measurements were carried out on the LF$_x$M$_{1-x}$P@C cathodes at different sweep rates from 0.05 to 0.5 mV s^{-1}. Generally, as the ratio of Fe/Mn increasing, the redox peaks become sharp. The LMP@C shows obvious polarization between the oxidation and reduction peaks (O$_{Mn}$ and R$_{Mn}$) corresponding to Mn^{2+}/Mn^{3+} redox couple at ca. 4.1 V (vs. Li/Li$^+$, Fig. 4a). Two pairs of current peaks associated with the Fe^{2+}/Fe^{3+} and Mn^{2+}/Mn^{3+} redox couples are present in LF$_x$M$_{1-x}$P@C (x = 0.25, 0.5, 0.75) (Fig. 4b−d). The LFP@C shows only the sharp oxidation and reduction peaks of Fe^{2+}/Fe^{3+} redox couple at ca. 3.5 V (vs. Li/Li$^+$) (Fig. 4e). Fig. 4f shows CV curves of the samples recorded at a fixed sweep rate of 0.05 mV s^{-1}. From this profiles, we calculate the potential difference (ΔE_P) between the oxidation and reduction peaks of the Fe^{2+}/Fe^{3+} and Mn^{2+}/Mn^{3+}, respectively. LF$_{0.5}$M$_{0.5}$P@C shows the Fe^{2+}/Fe^{3+} has the lowest ΔE_P (55 mV) and the Mn^{2+}/Mn^{3+} has a relatively low ΔE_P (116 mV) (Fig. 4f inset). The low polarization degree suggests a fast Li-ion diffusion kinetic behavior of LF$_{0.5}$M$_{0.5}$P@C [36]. The ΔE_P of Fe^{2+}/Fe^{3+} is smaller compared with that of Mn^{2+}/Mn^{3+} for all of these composites, indicating the intercalation/deintercalation associated with the Fe system is more reversible compared to the Mn system.

D$_{Li}$ is estimated according to the Randles-Sevcik equation (eqn (1)) [37]:

$$I_P = 2.69 \times 10^5 \, AC_{Li}D_{Li}^{1/2}n^{3/2}v^{1/2} \tag{1}$$

Where I_P is the peak current (A), A is the electrode area (cm^2), C$_{Li}$ is the molar concentration of Li$^+$ in LF$_x$M$_{1-x}$P. The unit cell volume of LF$_x$M$_{1-x}$P is calculated to be "a (6.1000 Å) × b (10.4600 Å) × c

(4.7440 Å) = 302.70 × 10^{-24} cm^3", thereby, 1 cm^3 contains 1/ (302.70 × 10^{-24}) = 3.30 × 10^{21} unit cells. Since every LF$_x$M$_{1-x}$P cell contains four Li$^+$, 1 cm^3 contains 4 × 3.30 × 10^{21}/ (6.02 × 10^{23}) = 2.20 × 10^{-2} mol Li$^+$. It means the Li$^+$ concentration is approximately 2.20 × 10^{-2} mol cm^{-3} [38]. D$_{Li}$ is the Li$^+$ diffusion coefficient at 298 K, n is the number of electrons involved in the redox process (n = 1 for Fe^{2+}/Fe^{3+} or Mn^{2+}/Mn^{3+} redox pair), and v is the sweep rate (V s^{-1}). The peak currents (I_P) versus the square root of sweep rates (v$^{1/2}$) plotted in Fig. S3. The corresponding D$_{Li}$ values versus the Fe doping amount is shown in Fig. 5a. With the doping amount of Fe increases, the D$_{Li}$ for redox reactions of Fe^{2+}/Fe^{3+} increases gradually. For that of Mn^{2+}/Mn^{3+}, the D$_{Li}$ shows a respective high value of 2.38 × 10^{-12} and 3.31 × 10^{-12} cm^2 s^{-1} upon the charge and discharge processes when x = 0.5.

In addition, we examined the electrode reaction kinetics through CV using the relationship between the measured peak current (I_P) and the scan rates (v) by the following eqn (2) [39–42]:

$$I_P = av^b \tag{2}$$

Where I_P and v obey a power law. Both a and b are adjustable parameters and b-values are derived from the slope of the curve of logI_P versus logv on the basis of eqn (3):

$$\log I_P = b \times \log v + \log a \tag{3}$$

The value of b is positively correlated with the corresponding Li$^+$ diffusion, determined from the slope of the plot of logI_P vs logv, where a higher b value suggests a faster reaction kinetics [42]. Based on the logI_P versus logv plots show in Fig. S4, Fig. 5b shows that the b value changes with the amount of Fe doping, suggesting that the increase of Fe doping amount has a positive effect on the reduction reaction of Mn. While it has a negative effect on the oxidation reaction of Mn and the redox reaction of Fe. In addition, the high D$_{Li}$ of the LF$_{0.5}$M$_{0.5}$P@C cathode can be rationally ascribed to its lower charge transfer resistance (R$_{ct}$) and higher electronic/
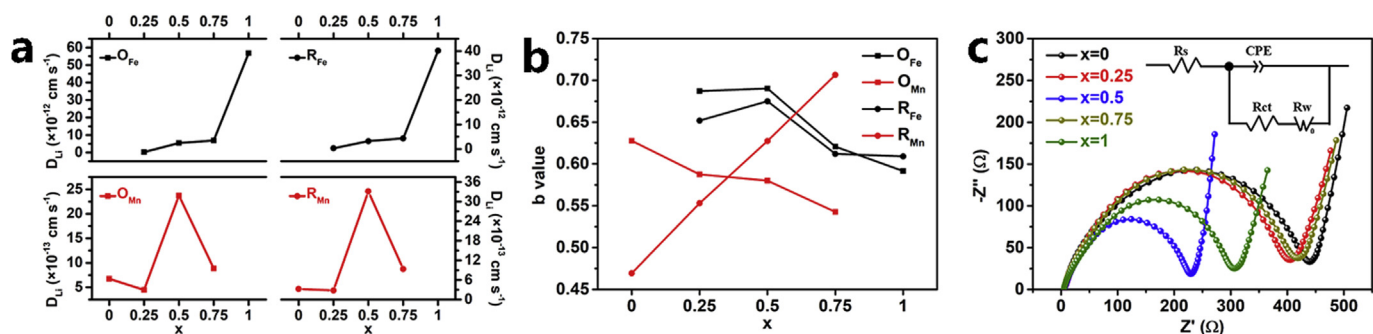
Fig. 5. (a) The D_{Li} values and (b) b values for redox reactions of Fe and Mn. (c) The Nyquist plots of LF$_x$M$_{1-x}$P@C electrodes with the inset showing the corresponding equivalent circuit. (A colour version of this figure can be viewed online.)

ionic conductivities than other LF$_x$M$_{1-x}$P@C, as evidenced from the Nyquist plots in Fig. 5c. The simulated values of EIS by using the equivalent circuit model (Fig. 5c inset) are summarized in Table S2. The solution resistance (R$_s$) value decreases as the amount of doping increases, whereas R$_{ct}$ is the smallest at x = 0.5. In addition to R$_{ct}$, the values of σ is calculated from the inclined lines in the Warburg region using the following eqn (4) [43]:

$$Z' = R_s + R_{ct} + \sigma\omega^{-1/2} \tag{4}$$

σ is equal to the slope of the straight line between Z' and $\omega^{-1/2}$, a smaller σ value implies a faster diffusion kinetics, as illustrated in Fig. S5. The σ determined from slopes of the linear fitting are summarized in Table S2. Accordingly, the σ is calculated to be 67.38, 72.53, 37.42, 68.79 and 57.02 Ω s$^{-1/2}$ for LMP@C, LF$_{0.25}$M$_{0.75}$P@C, LF$_{0.5}$M$_{0.5}$P@C, LF$_{0.75}$M$_{0.25}$P@C and LFP@C, respectively. Persuasively, the lower R$_{ct}$ and σ demonstrate that the proper doping amount is extremely important for efficient charge storage.

The electrochemical performance of the LF$_x$M$_{1-x}$P@C with galvanostatic charge-discharge cycles is shown in Fig. 6. The reversible

capacity of LF$_{0.5}$M$_{0.5}$P@C is 136.56 mAh g^{-1} after 100 cycles at 0.2 C, which is higher than that of LMP@C (70.37 mAh g^{-1}), LF$_{0.25}$M$_{0.75}$P@C (110.3 mAh g^{-1}), LF$_{0.75}$M$_{0.25}$P@C (118.53 mAh g^{-1}) and equivalent to LFP@C (137.06 mAh g^{-1}). LF$_{0.5}$M$_{0.5}$P@C also exhibits the highest columbic efficiency (CE) of near 100% after the initial cycles (Fig. 6a). The representative charge—discharge curves at 100th (Fig. 6b) shows that the LFP@C and LMP@C exhibiting one pair of voltage plateau at ~3.4 V and ~4.0 V, respectively. Whereas the LF$_x$M$_{1-x}$P (x = 0.25, 0.5, 0.75) exhibit the voltage plateaus of both the Fe^{2+}/Fe^{3+} and Mn^{2+}/Mn^{3+} redox couples. The results suggest that the LF$_{0.5}$M$_{0.5}$P@C exhibiting a cycling performance comparable to LFP@C but with a higher energy density due to a higher average working potential. At 0.2 C, LF$_{0.5}$M$_{0.5}$P@C electrode exhibits an energy density of 159 Wh kg^{-1} based on the mass of active substance, which is higher than that of LFP@C (131 Wh kg^{-1}). The increase in electrochemical activity on substituting Fe for Mn can be attributed to the improved electronic conductivity and lithium-ion conductivity compared to LMP. The crystalline stability of the LF$_x$M$_{1-x}$P@C electrodes after 100 cycles were characterized by XRD (Fig. S6a). All diffraction peaks of the samples can be indexed
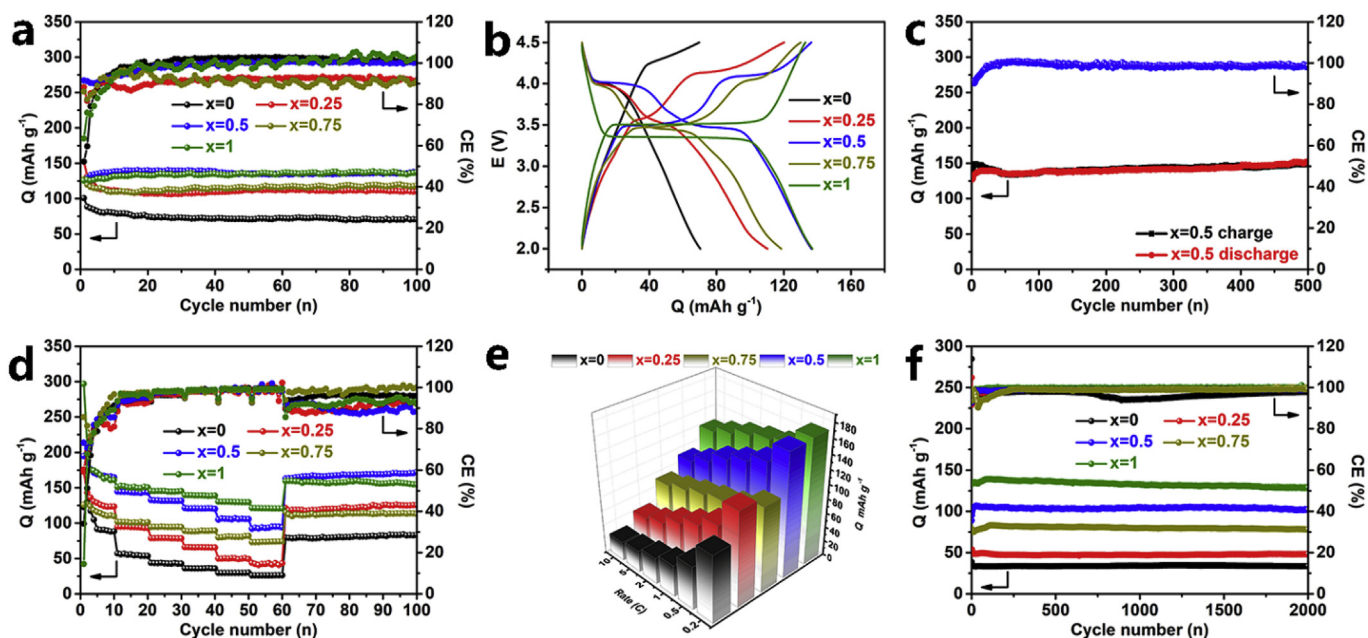

Fig. 6. Electrochemical performance of LF$_x$M$_{1-x}$P@C electrodes. (a) Cycling profiles with respect to specific capacity (Q) and coulombic efficiency (CE) at 0.2 C (1 C = 170 mA g^{-1}). (b) The representative voltage-capacity profiles at the 100th cycle. (c) Cycling profiles with respect to Q and CE of LF$_{0.5}$M$_{0.5}$P@C over 500 cycles at 0.2 C. (d) The rate capability at various current rates from 0.2 to 10 C. (e) The 3D comparison chart of the corresponding rate capability. (f) Cycling profiles with respect to Q and CE of LF$_x$M$_{1-x}$P@C electrodes up to 2000 cycles at 5 C. (A colour version of this figure can be viewed online.)

to an olivine-type structure with a Pnmb space group of LMP (JCPDS#74−0375) or LFP (JCPDS#83−2029) except that attributed to carbon (25°) and Al foil (65° and 78°). This also reasonably explains the long cycle stability of the material. Similar as that of pristine electrodes, all peaks in the XRD pattern of cycled $LF_xM_{1-x}P@C$ right shift as the doping amount increasing (Fig. S6b), indicating the structural stability.

The longer-term cycling performance of $LF_{0.5}M_{0.5}P@C$ shown in Fig. 6c clearly demonstrates the gradually increased capacity with cycling. A specific capacity of 150 mAh g^{-1} can be reached after 500 cycles with a capacity retention of 119%. Nearly steay-state charge−discharge profiles are present during the cycles (Fig. S7a). Highly overlapped two pair of current peaks that attributed to the Fe^{2+}/Fe^{3+} and Mn^{2+}/Mn^{3+} redox pairs exist in the CV curves at a sweep rate of 0.05 mV s^{-1} for repeated 10 cycles (Fig. S7b) without significant peak shift, indicating the high reversibility. Fig. 6d presents the rate capabilities of the $LF_{1-x}M_xP@C$ samples at the current rate of 0.2−10 C. As the current densities stepwise increased from 0.2 to 0.5, 1, 2, 5 and 10 C, the $LF_{0.5}M_{0.5}P@C$ delivers a stable capacities of 169, 144, 131.6, 121, 105, 93 mAh g^{-1} on the respective 5th cycle of each current density, respectively. In spite the rate capability is not better than that of LFP@C, a high capability of 163 mAh g^{-1} can be recovered rapidly from 10 to 0.2 C when continue to 100 cycles, exhibiting a strong tolerance of the rapid Li$^+$ insertion/extraction. The 3D rate capability chart more clearly demonstrates the gradually increased capacity at each rate with increasing the Fe doping from x = 0 to 0.75. The high-rate longer-term cycling performance of $LF_xM_{1-x}P@C$ at 5 C is shown in Fig. 6f. Impressively, a specific capacity of 102 mAh g^{-1} for $LF_{0.5}M_{0.5}P@C$ can still be afforded after 2000 cycles with ~100% CE. Such an overall electrochemical performance of $LF_{0.5}M_{0.5}P@C$ is among the top results of LMP/LFP hybrid systems [8,13,20−23,44,45]. A comparison of the synthesis route, material morphology, Fe/Mn ratio and electrochemical performance between this work and the previous reports is shown in Table S3. In a careful review of previous reports [8,13,20−23,44,45], it can be seen the synthesis route that determine the material morphology and Fe/Mn ratio that associated with the Li$^+$ diffusion speed are critical factors that affect the cell performance.

4. Conclusions

To sum up, fibrous $LF_xM_{1-x}P@C$ (x = 0, 0.25, 0.5, 0.75, 1) cathode materials were synthesized via a feasible electrospinning followed by a simple heat-treatment. XRD and EDS characterizations confirm the uniform substitution of Fe at Mn site in the olivine structure, leading to an increased Li diffusion kinetics. The $LF_{0.5}M_{0.5}P@C$ holds the largest D_{Li} value of 2.38×10^{-12} and 3.31×10^{-12} cm^2 s^{-1}, respectively, for the charge and discharge processes. At a low current rate of 0.2 C, a specific capacity of 150 mAh g^{-1} can be kept after 500 cycles without any capacity loss. At a high rate of 5 C, remarkable rate capability and cycling stability are achieved for a longer-term cycling of 2000 cycles. The outstanding electrochemical performance of $LF_{0.5}M_{0.5}P@C$ is attributed to two main reasons. Firstly, the 3D networks of 1D nanofibers with conductive carbon matrix significantly improves the ionic and electronic transport. More importantly, the proper amount of Fe-substituted Mn greatly increases the D_{Li}, leading to the quick charge at high rates.

Declaration of competing interestCOI

The authors declare no competing financial interest.

Appendix A. Supplementary data

Supplementary data to this article can be found online at https://doi.org/10.1016/j.carbon.2019.11.067.

References

[1] M. Armand, J.-M. Tarascon, Building better batteries, Nature 451 (2008) 652−657.
[2] P.G. Bruce, B. Scrosati, J.-M. Tarascon, Nanomaterials for rechargeable lithium batteries, Angew. Chem. Int. Ed. 47 (2008) 2930−2946.
[3] T.-W. Zhang, T. Tian, B. Shen, Y.-H. Song, H.-B. Yao, Recent advances on biopolymer fiber based membranes for lithium-ion battery separators, Compos. Commun. 14 (2019) 7−14.
[4] Y. Zou, S. Chen, X. Yang, N. Ma, Y. Xia, D. Yang, et al., Suppressing Fe−Li antisite defects in LiFePO4/Carbon hybrid microtube to enhance the lithium ion storage, Adv. Energy Mater. (2016), 1601549.
[5] C. Sun, S. Rajasekhara, J.B. Goodenough, F. Zhou, Monodisperse porous LiFePO4 microspheres for a high power Li-ion battery cathode, J. Am. Chem. Soc. 133 (2011) 2132−2135.
[6] K. Saravanan, P. Balaya, M.V. Reddy, B.V.R. Chowdari, J.J. Vittal, Morphology controlled synthesis of LiFePO4/C nanoplates for Li-ion batteries, Energy Environ. Sci. 3 (2010) 457−464.
[7] A.K. Padhi, K.S. Nanjundaswamy, J.B. Goodenough, Phospho-olivines as positive-electrode materials for rechargeable lithium batteries, J. Electrochem. Soc. 144 (1997) 1188−1194.
[8] Y. Wang, C.-Y. Wu, H. Yang, J.-G. Duh, Rational design of a synthetic strategy, carburizing approach and pore-forming pattern to unlock the cycle reversibility and rate capability of micro-agglomerated LiMn0.8Fe0.2PO4 cathode materials, J. Mater. Chem. A 6 (2018) 10395−10403.
[9] Y.H. Jung, W.B. Park, M. Pyo, K.-Sun Sohn, D. Ahn, A multi-element doping design for a high-performance LiMnPO4 cathode via metaheuristic computation, J. Mater. Chem. A 5 (2017) 8939−8945.
[10] J. Hu, W. Xiao, H. Tang, H. Wang, Z. Wang, C. Liu, et al., Tuning Li-ion diffusion in α-LiMn1−xFexPO4 nanocrystals by antisite defects and embedded β-phase for advanced Li-ion batteries, Nano Lett. 17 (2017) 4934−4940.
[11] S. Wi, J. Park, S. Lee, J. Kim, B. Gil, A.J. Yun, et al., Insights on the delithiation/lithiation reactions of LixMn0.8Fe0.2PO4 mesocrystals in Li$^+$ batteries by in situ techniques, Nano Energy 39 (2017) 371−379.
[12] X. Fu, K. Chang, B. Li, H. Tang, E. Shangguan, Z. Chang, Low-temperature synthesis of LiMnPO4/RGO cathode material with excellent voltage platform and cycle performance, Electrochim. Acta 225 (2017) 272−282.
[13] F. Wen, T. Lv, P. Gao, B. Wu, Q. Liang, Y. Zhang, et al., Graphene-embedded LiMn0.8Fe0.2PO4 composites with promoted electrochemical performance for lithium ion batteries, Electrochim. Acta 276 (2018) 134−141.
[14] M.K. Devaraju, I. Honma, Hydrothermal and solvothermal process towards development of LiMPO4 (M = Fe, Mn) nanomaterials for lithium-ion batteries, Adv. Energy Mater. 2 (2012) 284−297.
[15] Y.-K. Hou, G.-L. Pan, Y.-Y. Sun, X.-P. Gao, LiMn0.8Fe0.2PO4/Carbon nanospheres@graphene nanoribbons prepared by the biomineralization process as the cathode for lithium-ion batteries, ACS Appl. Mater. Interfaces 10 (2018) 16500−16510.
[16] L. Liang, X. Sun, J. Zhang, L. Hou, J. Sun, Y. Liu, et al., In situ synthesis of hierarchical core double-shell Ti-doped LiMnPO4@NaTi2(PO4)3@C/3D graphene cathode with high-rate capability and long cycle life for lithium-ion batteries, Adv. Energy Mater. (2019), 1802847.
[17] B. Wang, T. Liu, A. Liu, G. Liu, L. Wang, T. Gao, et al., A hierarchical porous C@LiFePO4/Carbon nanotubes microsphere composite for high-rate lithium-ion batteries: combined experimental and theoretical study, Adv. Energy Mater. 6 (2016), 1600426.
[18] S. Li, X. Meng, Q. Yi, J.A. Alonso, M.T. Fernández-Díaz, C. Sun, et al., Structural and electrochemical properties of LiMn0.6Fe0.4PO4 as a cathode material for flexible lithium-ion batteries and self-charging power pack, Nano Energy 52 (2018) 510−516.
[19] W. Huang, J. Hu, L. Yang, W. Zhao, Z. Wang, H. Wang, et al., Revealing the degradation mechanism of LiMnxFe1−xPO4 by the single-particle electrochemistry method, ACS Appl. Mater. Interfaces 11 (2019) 957−962.
[20] M. Zhao, G. Huang, B. Zhang, F. Wang, X. Song, Characteristics and electrochemical performance of LiFe0.5Mn0.5PO4/C used as cathode for aqueous rechargeable lithium battery, J. Power Sources 211 (2012) 202−207.

[21] H. Liu, L. Ren, J. Li, H. Tuo, Iron-assisted carbon coating strategy for improved electrochemical LiMn$_{0.8}$Fe$_{0.2}$PO$_4$ cathodes, Electrochim. Acta 212 (2016) 800−807.

[22] K. Saravanan, V. Ramar, P. Balaya, J.J. Vittal, Li(Mn$_x$Fe$_{1-x}$)PO$_4$/C (x=0.5, 0.75 and 1) nanoplates for lithium storage application, J. Mater. Chem. 21 (2011) 14925−14935.

[23] W. Xiang, E.-H. Wang, M.-Z. Chen, H.-H. Shen, S.-L. Chou, H. Chen, et al., Hierarchical structured LiMn$_{0.5}$Fe$_{0.5}$PO$_4$ spheres synthesized by template-engaged reaction as cathodes for high power Li-ion batteries, Electrochim. Acta 178 (2015) 353−360.

[24] C. Portet, G. Yushin, Y. Gogotsi, Electrochemical performance of carbon onions, nanodiamonds, carbon black and multiwalled nanotubes in electrical double layer capacitors, Carbon 45 (2007) 2511−2518.

[25] L.-H. Hu, F.-Y. Wu, C.-T. Lin, A.N. Khlobystov, L.-J. Li, Graphene-modified LiFePO$_4$ cathode for lithium ion battery beyond theoretical capacity, Nat. Commun. 4 (2013) 1687.

[26] X. Tu, Y. Zhou, X. Tian, Y. Song, C. Deng, H. Zhu, Monodisperse LiFePO$_4$ microspheres embedded with well-dispersed nitrogen-doped carbon nanotubes as high-performance positive electrode material for lithium-ion batteries, Electrochim. Acta 222 (2016) 64−73.

[27] B. Wang, W.A. Abdulla, D. Wang, X.S. Zhao, A three-dimensional porous LiFePO$_4$ cathode material modified with a nitrogen-doped graphene aerogel for high-power lithium ion batteries, Energy Environ. Sci. 8 (2015) 869−875.

[28] J.-W. Leea, M.-S. Parka, B. Anass, J.-H. Parka, M.-S. Paika, S.-G. Doo, Electrochemical lithiation and delithiation of LiMnPO$_4$: effect of cation substitution, Electrochim. Acta 55 (2010) 4162−4169.

[29] Z.P. Lu, X.J. Lu, J.J. Ding, T. Zhou, T. Ge, G. Yang, et al., Enhanced electrochemical performance of LiMn$_2$O$_4$ by constructing a stable Mn^{2+}-rich interface, Appl. Surf. Sci. 426 (2017) 19−28.

[30] Z.H. Xiao, Y. He, X.L. Li, L.Y. Zhang, Z.Q. Ding, Enhanced electrochemical performances of LiMnPO$_4$/C via liquid crystal template pathway, ChemistrySelect 3 (2018) 4222−4227.

[31] J.G. Zheng, L. Ni, Y.W. Lu, C.C. Qin, P.X. Liu, T.F. Wu, et al., High-performance, nanostructure LiMnPO$_4$/C composites synthesized via one-step solid state reaction, J. Power Sources 282 (2015) 444−451.

[32] Y. Gao, L. Zhang, S. Feng, W. Shen, S. Guo, Improving the electrochemical properties of lithium iron(II) phosphate through surface modification with manganese ion(II) and reduced graphene oxide, J. Solid State Electrochem. 22 (2018) 285−292.

[33] C. Gao, J. Zhou, G. Liu, L. Wang, Lithium-ions diffusion kinetic in LiFePO$_4$/ carbon nanoparticles synthesized by microwave plasma chemical vapor deposition for lithium-ion batteries, Appl. Surf. Sci. 433 (2018) 35−44.

[34] C.X. Zhao, Y. Zhang, S.Z. Deng, N.S. Xu, J. Chen, Surface nitrogen functionality for the enhanced field emission of freestanding few-layer graphene nanowalls, J. Alloy. Comp. 672 (2016) 433−439.

[35] B.J. Tan, K.J. Klabunde, P.M.A. Sherwood, XPS studies of solvated metal atom dispersed catalysts. evidence for layered cobalt-manganese particles on alumina and silica, J. Am. Chem. Soc. 113 (1991) 855−861.

[36] Y. Zhang, Y. Huang, Y. Tang, H. Zhao, Y. Cai, X. Wang, et al., Improved rate capability and cycling stability of bicontinuous hierarchical mesoporous LiFePO$_4$/C microbelts for lithium-ion batteries, New J. Chem. 41 (2017) 12969−12975.

[37] Y. Zhao, L. Peng, B. Liu, G. Yu, Single-crystalline LiFePO$_4$ nanosheets for high-rate Li-ion batteries, Nano Lett. 14 (2014) 2849−2853.

[38] J.-Z. Guo, P.-F. Wang, X.-L. Wu, X.-H. Zhang, Q. Yan, H. Chen, et al., High-energy/power and low-temperature cathode for sodium-ion batteries: in situ XRD study and superior full-cell performance, Adv. Mater. 29 (2017), 1701968.

[39] H. Lindström, S. Södergren, A. Solbrand, H. Rensmo, J. Hjelm, A. Hagfeldt, et al., Li$^+$ ion insertion in TiO$_2$ (Anatase). 2. voltammetry on nanoporous films, J. Phys. Chem. B 101 (1997) 7717−7722.

[40] P. Simon, Y. Gogotsi, B. Dunn, Where do batteries end and supercapacitors begin? Science 34 (2014) 1210−1211.

[41] X. Dong, L. Chen, J. Liu, S. Haller, Y. Wang, Y. Xia, Environmentally-friendly aqueous Li (or Na)-ion battery with fast electrode kinetics and super-long life, Sci. Adv. 2 (2016), e1501038.

[42] Y. Tao, Y. Wei, Y. Liu, J. Wang, W. Qiao, L. Ling, et al., Kinetically-enhanced polysulfide redox reactions by Nb$_2$O$_5$ nanocrystals for high-rate lithium-sulfur battery, Energy Environ. Sci. 9 (2016) 3230−3239.

[43] D. Saikia, J.R. Deka, C.-J. Chou, C.-H. Lin, Y.-C. Yang, H.-M. Kao, Encapsulation of LiFePO$_4$ nanoparticles into 3D interpenetrating ordered mesoporous carbon as a high-performance cathode for lithium-ion batteries exceeding theoretical capacity, ACS Appl. Energy Mater. 2 (2019) 1121−1133.

[44] S.-B. Yang, J.-T. Son, Enhanced rate-capability of a highly homogeneous polyaniline coating for LiFe$_{0.8}$Mn$_{0.2}$PO$_4$ nanofibers, J. Nanosci. Nanotechnol. 16 (2016) 10654−10658.

[45] B.Z. Li, Y. Wang, L. Xue, X.P. Li, W.S. Li, Acetylene black-embedded LiMn$_{0.8}$Fe$_{0.2}$PO$_4$/C composite as cathode for lithium ion battery, J. Power Sources 232 (2013) 12−16.